Structural and magnetic confinement of holes in the spin-polarized emission of coupled quantum ring–quantum dot chains

Vivaldo Lopes-Oliveira,[1] Yuriy I. Mazur,[2] Leonardo Dias de Souza,[1] Lucas A. Bernardes Marçal,[3] Jiang Wu,[4]
Marcio Daldin Teodoro,[1] Angelo Malachias,[3] Vitaliy G. Dorogan,[2] Mourad Benamara,[2] Georgiy G. Tarasov,[5]
Euclydes Marega, Jr.,[6] Gilmar E. Marques,[1] Zhiming M. Wang,[7] Milan Orlita,[8] Gregory J. Salamo,[2] and Victor Lopez-Richard[1]

[1]*Departamento de Física, Universidade Federal de São Carlos, 13565-905 São Carlos, SP, Brazil*
[2]*Arkansas Institute for Nanoscale Materials Science and Engineering, University of Arkansas, Fayetteville, Arkansas 72701, USA*
[3]*Departamento de Física, Universidade Federal de Minas Gerais, 31270-010 Belo Horizonte, Minas Gerais, Brazil*
[4]*State Key Laboratory of Electronic Thin Film and Integrated Devices, University of Electronic Science and Technology of China,
Chengdu, People's Republic of China*
[5]*Institute of Semiconductor Physics, National Academy of Sciences, pr. Nauki 45, Kiev-03028, Ukraine*
[6]*Instituto de Física de São Carlos, Universidade de São Paulo, 13.566-590 São Carlos, São Paulo, Brazil*
[7]*Institute of Fundamental and Frontier Sciences, University of Electronic Science and Technology of China,
Chengdu 610054, People's Republic of China*
[8]*Laboratoire National des Champs Magnétiques Intenses, CNRS-UJF-UPS-INSA, Grenoble 38042, France*

The optical analysis of multilayer structures formed from the topmost layer of InGaAs/GaAs quantum rings (QRs) grown on a vertically stacked and laterally aligned InGaAs/GaAs quantum dot (QD) superlattice has been performed to elucidate the nature of the contribution from each layer. These hybrid structures representing a coupled QR chain layer and the layers of self-assembled QD chains display strong optical anisotropy. Unusually strong oscillations are observed in the circularly polarized photoluminescence (PL) intensities under magnetic field for emissions in the spectral range of the QD structure and these oscillations occur simultaneously with weaker oscillations related to the Aharonov-Bohm interference that modulates the emissions from the QR top layer of the structure. The behavior seen in the magneto-PL spectrum is interpreted in terms of joint effects associated to strain, spatial, and magnetic field confinements on the valence band states forming the magnetoexciton ground state of this multilayered structure. The result can be ascribed to a magnetically induced dark exciton contribution where the heavy-hole (type II) state becomes localized outside, whereas light-hole (type I) as well as electron states remain inside the spatial confinement area of the QD.

I. INTRODUCTION

Nowadays, the advances in growth techniques have resulted in a wide spectrum of nanoscale structures suitable for various applications. Different ordered nanostructures such as dot chains, quantum wires, nanorods, nanogrids, nanodroplets, and nanopillars were already realized [1–8]. In these structures, a flexible engineering of wave function of confined carriers is possible by controlling the overlap between adjacent nano-objects via changes of the space between them [1–3,9].

Very recently, laterally ordered quantum ring chains were fabricated by using the conventional Stranski-Krastanov growth mode [10,11] and attracted both theoretical and experimental interest [12,13]. This method has become the main recipe for fabricating ordered arrays of quantum dots and rings. To attain self-organization of nanoscopic structures with the highest possible uniformity and geometry control, a layer-by-layer growth is indispensable. Unavoidably, a vertical stack of nanoscopic islands is formed in this process. Thus, even when the final goal of a growth is, for instance, the production of ordered quantum rings, the analysis of the potential interference of the subjacent structures in the optical response becomes a paramount need. Thus, we have set two main objectives to be tackled in this work: to elucidate the nature of each contribution to the magneto-optical emission of this kind of system while understanding and contrasting

their differences and to point out the dominant effects. In order to attain these goals, a combination of experimental and theoretical procedures has been gathered to build an accurate framework for the analysis. A versatile model was used to calculate the electronic structure of the valence band. This model provides an analytical solution in the in-plane problem for the quantum ring and the quantum dot, just by parameters changing and accounts for realistic symmetry reduction as perturbations in the presence of magnetic field and strain.

Due to the vertical stacking that produces the self-assembling from the quantum dot (QD) seeds to the quantum rings (QRs) and their lateral alignment, it becomes imperative to assess the relative contribution of each mode to the optical response, since their geometries and strain field propagation may affect the responses differently. Thus, the electronic structure, in particular in the valence band, where anisotropy and deformation potentials are so crucial, must be accounted for. We will show that these effects can be enhanced by the application of a magnetic field.

It has been predicted [13] that the in-plane radial polarization of excitons in finite-width QRs can produce a strong modulation of the oscillator strength of the excitonic transition with magnetic field, due to a topologically determined quantum interference known as the Aharonov-Bohm (AB) effect [13–17]. The AB interference in type-I systems, where both electron and hole move together inside the ring, has

been found in the magneto-PL (photoluminescence) from self-assembled InGaAs/GaAs QR single layer structures [16]. It has also been shown that optical emissions from type-II ZnTe/ZnSe QDs display large and persistent oscillations in both peak energy and intensity, thus indicating the formation of coherently rotating states in magnetic fields [13,18].

In this work, we investigate a hybrid type of structure where one layer of InGaAs/GaAs QRs is grown on a vertical superlattice of InGaAs/GaAs QDs aligned laterally. This hybrid ensemble of nanostructures reveals strong optical anisotropy in the polarized PL spectrum and unusually strong oscillations of PL intensities as a function of magnetic field in both QD and QR spectral emission ranges. These oscillations are observed simultaneously and related to the Aharanov-Bohm interference patterns. Such behavior of the magneto-PL can be understood in terms of joint effects associated to strain, spatial, and magnetic confinements affecting the valence band states forming the magnetoexciton ground state of the hybrid structure.

II. STRUCTURAL CHARACTERIZATION

Our samples were grown in a molecular beam epitaxy chamber on semi-insulating GaAs(001) substrates. (For more detailed information, see Refs. [10,11].) They are composed of multiple layers of $In_{0.4}Ga_{0.6}As$ QDs separated by capping GaAs barriers with the top layer consisting of InGaAs QRs, and are displayed in the atomic force microscopy (AFM) images in Figs. 1(a) and 1(b). The ring-shaped InGaAs nanostructures are clearly preserving the lateral ordering of the seed InGaAs QDs chains along the [1$\bar{1}$0] direction. The capping layer thickness separating the dot structures was 4 nm for this sample. As shown in Ref. [4], the regularity and length of QR chains can be improved with lower InGaAs coverage and with the introduction of additional growth interruption times. A morphological and structural analysis of this hybrid QR-QD sample was carried out using a FEI Titan 80-300 transmission electron microscope (TEM) and displayed distinctly the vertically ordered $In_{0.4}Ga_{0.6}As$/GaAs QD layers topped with the final InGaAs/GaAs QR layer, as seen in the left side of Fig. 1(b). The TEM analysis indicates that the rings have an average diameter of 31.5 ± 4.5 nm and a height of 3.0 nm with an areal density of $\sim 7.9 \times 10^9$ cm^{-2}, whereas the low-lying dots have a smaller average diameter of 15 nm and a height of 6.0 nm with an areal density of $\sim 1 \times 10^{10}$ cm^{-2}. The rings are larger than dots due to the strong outer diffusion of materials during the dot-to-ring transformation growth process [11].

In order to obtain realistic strain profiles inside the QD and QR layers of our hybrid structure, we used a commercial software package to simulate nanostructures by the finite-element method (FEM). The mechanical strain used is anisotropic. The commercial FEM platform (COMSOL) used in this work has a full library of mechanical properties of semiconductors and is able to provide a full description of III-V systems, in which properties such as Young's modulus, Poisson's ratio, and shear modulus vary accordingly from one main crystallographic direction to another. The modeling is carried out ascribing the main crystallographic axes to the FEM geometry axis. In our case, the [001] direction was ascribed to the *z* (growth/stack) axis, while in-plane [100] and [010] directions lie on the *x*
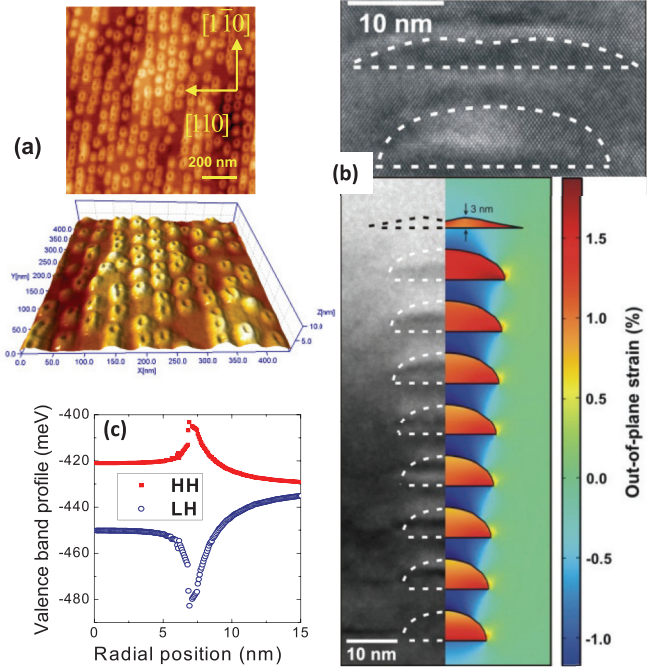

FIG. 1. (Color online) (a) AFM image of the topmost layer containing QR chains grown on an $In_{0.4}Ga_{0.6}As$/GaAs(001) vertical QD superlattice. (b) Left side: Multibeam bright field TEM images of the hybrid multilayered sample used in this work. Right side: The FEM model of the QD/QR stack. For the out-of-plane strain in color code shown on the right, the blue colors are related to compressive (negative) out-of plane strain while green/yellow/red colors denote tensile (positive) out-of-plane strain. Top: High-resolution TEM image of the last two top layers. (c) Calculated valence band deformation potential profiles for repulsive heavy-hole (HH) and attractive light-hole (LH) carriers in the QD region. The position axis represented in panel (c) depicts the coordinate along the radial [110] direction is on the vertical distance of 0.5 nm from the islands base plane, where $r = 0$ nm corresponds to the center of the dot.

and *y* coordinates (island base plane), respectively. Modeling with isotropic parameters was also performed (considering the elastic constants of the $\langle 100 \rangle$ planes for all positions) and deviations between both results were found to lie within a 10% discrepancy. In this case, lower strain values are found if the material is considered isotropic.

The QD and QR dimensions as well as morphologies were matched to the TEM observations and inserted into a GaAs matrix [19,20]. The In composition inside the QDs was fixed to 40% while at the QRs it was set to 25%. A lateral cut from the FEM results is shown in the right side of Fig. 1(b) superimposed to a TEM image of the QD/QR stack on the left side. The color code with green/yellow/red areas represents regions of the dots and rings subjected to tensile (positive) out-of-plane strain, due to pseudomorphic relaxation under in-plane compressive strain, while blue regions show areas subjected to compressive (negative) strain due to an in-plane lattice expansion associated to GaAs capping regions between QD layers. We have analyzed out-of-plane and in-plane strain profiles (considering the growth direction as [001]) along the QD stack. Our study also included a validation of the [001] strain profile monitoring out-of-plane and in-plane strain

profiles at the base of each QD along the [100], [010], and [110] directions (not shown in the paper for simplicity).

Strain profiles along selected directions are extracted from the FEM data and used for valence band deformation potential calculations as displayed in Fig. 1(c) for the lowest QD according to Ref. [21]. Note the difference between the heavy-hole (HH) and light-hole (LH) energy shifts that would ultimately lead to a difference in the character of the two hole confinement types. Since the HH states will be predominantly confined nearby the lateral QD boundary while the LH states occupy the internal dot region, then heavy-hole optical recombination will display a type-II character, whereas light-hole recombination displays a type-I character. We will prove that the light emission from the ground state excitons with type-II character is forbidden by selection rules, yet they have important influence in the detected PL emission. Although the strain fields built in the process of coherent formation of the quantum dots and rings lead to a structural link between the stack layers, the distance between them inhibits the electronic coupling. However, by rising temperatures beyond the cryogenic values used for the magneto-optical characterization, a net charge transfer can be put in place through hopping mechanisms activated by phonons.

The PL measurements were performed in a variable temperature, closed-cycle, helium cryostat using various laser sources as excitation. The laser spot diameter was $\sim$20 μm and the optical excitation power was kept in the range of 10^{-7}–10^2 mW. The PL signals from the sample were dispersed by a monochromator and detected by a liquid-nitrogen-cooled InGaAs photodiode array.

Figure 2(a) shows continuous wave PL spectra measured at different excitation wavelengths and normalized to the maximum PL peak values in each spectrum, with the lines being intentionally displaced vertically for clarity and easier comparison. Two bands, labeled QD at higher energy and QR at lower energy sides, can be identified. Figure 2(b) shows the relative integrated intensities, I_{QD}/I_{QR}. The relative contribution from the low energy emission band to the total low temperature spectrum increases if the excitation wavelength λ_{ex} is shortened. The band at $E = 1.079$ eV, is ascribed to ground state excitonic transition from the QR layer. On the contrary, the contribution from the high energy PL band, at $E = 1.179$ eV, increases if the λ_{ex} value is increased. This high energy band corresponds to excitonic transitions from the buried dot layers. While the absorption coefficient of our multilayered structure depends substantially on the radiation wavelength [22], a short wavelength radiation will be absorbed predominantly by the top QR layer. Therefore, short excitation wavelengths increase the QR contribution to the whole PL spectrum, as can be seen in Fig. 2(a), and reaches only a few buried top dot layers. The deeper the excitation reaches, the larger is the relative intensity difference between QR and QD emission signals. The lateral size of the QRs, as described in Ref. [23], compared to the QDs, will also lead to a shrinkage of the emission energy.

Besides the dot size difference of the dominant vertical stacking, our system is laterally anisotropic. The $In_{0.4}Ga_{0.6}As/GaAs$ QDs are aligned in chainlike structures and so are the rings in the top layer. In addition to the alignment along the [01$\bar{1}$] direction, the QRs, like the $In_{0.4}Ga_{0.6}As$
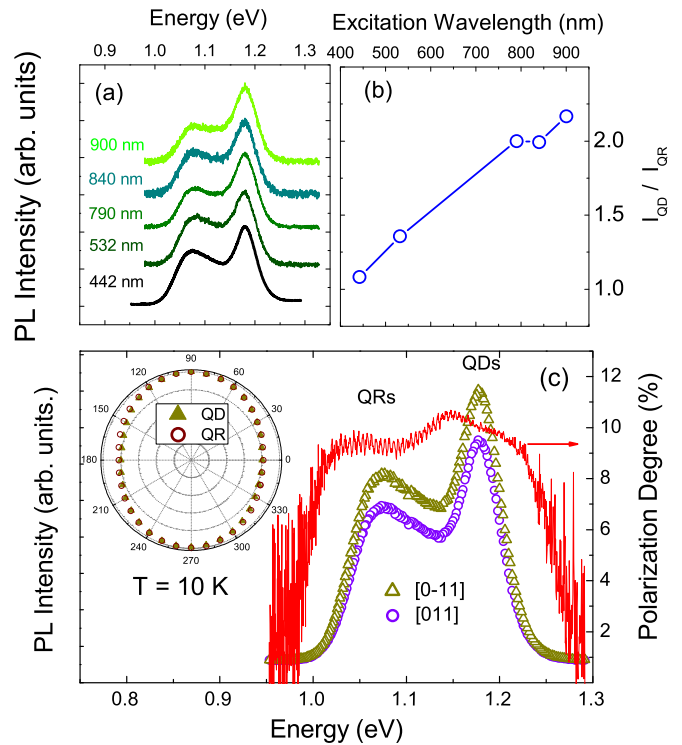

FIG. 2. (Color online) (a) PL spectra measured at different excitation wavelengths. (b) The relative integrated intensities, I_{QD}/I_{QR}, of dot and ring emission bands increases for increasing excitation wavelength once the deeper dot layers become excited. (c) Low temperature PL spectra, excited with $\lambda_{ex} = 442$ nm and excitation intensity $I_{ex} = 7$ W/cm^2, measured for two orthogonal polarizations: parallel to the [01$\bar{1}$] and [011] directions. A polar plot shown on the left, displays the angular anisotropy of the PL spectra as normalized to maximum value of the intensities for both the QD and QR emissions. Note also a degree of polarization near 10% for these emissions.

QDs, are slightly elongated with an elliptical shape along this direction. The reason for elongation of the QDs and QRs is the anisotropic diffusion of In adatoms and the anisotropy of surface free energies and elastic strain distribution. This anisotropy leads to differences on the linearly polarized emissions. Thus, the PL spectra from the QR-QD sample were measured at $T = 10$ K for two orthogonal polarizations: along the [01$\bar{1}$] and [011] directions. The spectra are shown in Fig. 2(c) together with the linear polarization degree defined as PD $= (I_{[01\bar{1}]} - I_{[011]})/(I_{[01\bar{1}]} + I_{[011]}) \times 100\%$, where $I_{[01\bar{1}]}$ and $I_{[011]}$ are the intensities of the emission polarized along the [01$\bar{1}$] and [011] directions, respectively. The angular dependence of the emission lines for both QDs and QRs is displayed in the polar plot that shows the normalized PL intensity to its maximum value as a function of the polarization direction. We detected a polarization degree at the maximum of QD and QR emissions of around 10%, for these typical elongated dots [24], as also displayed in Fig. 2(c).

III. MAGNETOPHOTOLUMINESCENCE

Magnetophotoluminescence measurements were performed at 4.2 K and with magnetic fields up to 21 T. A monomode optical fiber with 5 μm core was used to bring

the 640 nm excitation from a diode laser to the sample, with a focus of 1 μm spot and an excitation power of 1 mW. The luminescence from the sample was then collected by a multimode 200 μm optical fiber before being dispersed by a 0.5 m spectrometer and analyzed with a diffraction grating and a nitrogen-cooled CCD. A set of quarter-wave plates and linear polarizers, placed close to the sample were then used to circularly polarize the emissions. Both σ^- and σ^+ polarizations were analyzed by setting the quarter-wave plate in $+45^o$ for σ^+ with respect to the linear polarizer, and the corresponding σ^- component was obtained by changing the magnetic field to negative values.

For magneto-PL measurements, the emission signals were collected after using an excitation intensity $I_{ex} = 50$ W/cm^2, and the low temperature spectra for circular polarizations are shown in Fig. 3(a), for $B = 0$ T, and (b), for $B = 21$ T. Both lower and higher energy PL bands are blueshifted for increasing magnetic field, regardless of the type of polarized

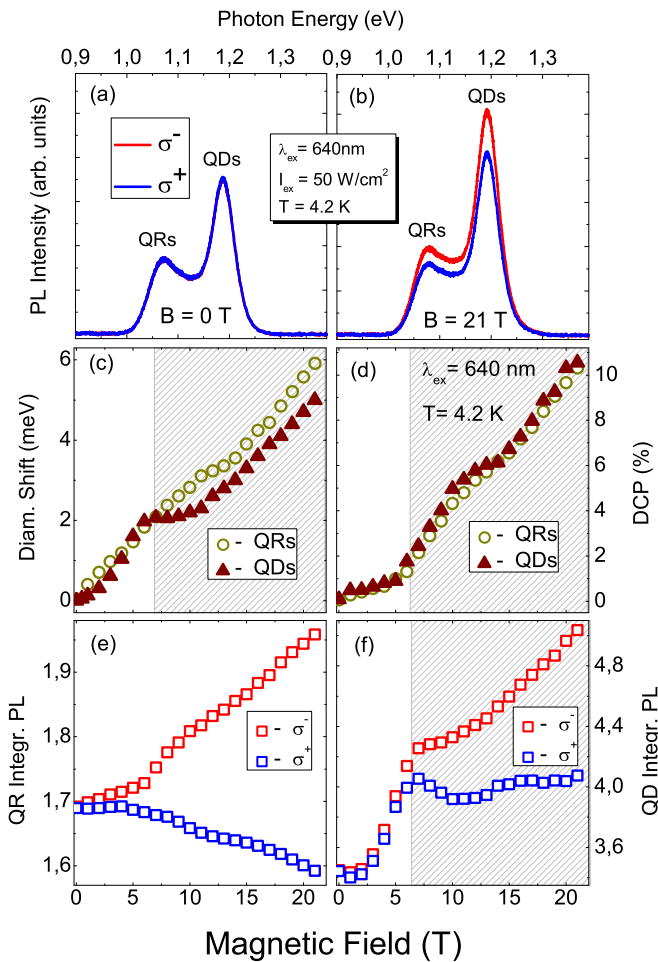FIG. 3. (Color online) (a), (b) Spectra excited with $\lambda_{ex} =$ 640 nm, excitation power $I_{ex} = 50$ W/cm^2 and measured for the circular polarizations σ^+ and σ^- in Faraday geometry for (a) $B = 0$ T and (b) $B = 21$ T. (c) Diamagnetic shift of the exciton ground state transitions versus magnetic field. (d) Degree of circular polarization measured at the peak energies, for QDs and QRs σ^+ and σ^- emissions. The integrated PL intensities for the hybrid sample, with σ^+ and σ^- polarizations measured in Faraday geometry, are shown for QRs (e) and QDs (f) as a function of magnetic field.

emission, although the PL intensities for QR (lower energy) and QD (higher energy) bands behave rather differently as the field is increased. The circular polarized anisotropy that arises, for finite magnetic fields, can be seen in Figs. 3(c) and 3(d). The diamagnetic shift, defined as $\Delta E_{\text{diam}} = [E^{\sigma^+}(B) + E^{\sigma^-}(B)]/2 - E(0)$, is shown in Fig. 3(c). The positive curvature is characteristic of a diamagnetic behavior and reveals a smooth dependence on the magnetic field up to ~6 T. By using a gray-shaded area we have highlighted a region where changes in the diamagnetic curvature can be noted for the QD emission (for field strengths above 6 T). It is seen that the PL emissions split into lower and upper branches due to the Zeeman effect for excitons under magnetic field. As reported in Ref. [25] for a very similar system, the value of Zeeman splitting shows linear dependence on B and displays a slope of $\simeq$120 μeV/T. By applying this rate to our QD-QR hybrid structure, we estimated the value for the Zeeman splitting on the order of 2.5 meV for $B = 21$ T in the sample. Taking into account the width $\simeq$50 meV of the PL bands for both QD and QR ensembles, we conclude that is not possible to resolve such a small splitting, in our case. Yet, the total shift to higher energies of the PL peak positions with applied field, behaves distinctly as seen in our experiments. For the QR emission line, no sudden changes can be identified in the peak position at the critical field $B_c = 6$ T, besides the subtle oscillations above B_c that are ascribed to the changes in the angular momentum of the ground state for increasing magnetic field [16]. The QD superlattice shows a discontinuity on the rate of change at 6 T and then, an almost quadratic increase above $B_c = 6$ T. However, the degree of circular polarization (DCP), although increasing for increasing B, displays equal rates for the QR and QD emission bands up to 21 T, as depicted in Fig. 3(d). The QR integrated $\sigma^\pm$ intensities, displayed in Fig. 3(e), also oscillate slightly displaying changes very similar to the diamagnetic shift behavior, although the integrated σ^+ intensities of QD and QR show rather different behavior inside and outside the gray-shaded area. The QR σ^+ intensity is almost constant below 6 T and then decreases gradually with increasing field, whereas the σ^+ intensity for the QD superlattice increases almost quadratically below 6 T and oscillates slightly around a constant value for fields above 6 T. These drastic changes in PL occurring at $B \sim 6$ T take place in the energy positions and PL intensities of the QD emission band.

IV. ELECTRONIC STRUCTURE

According to the structural characterization, two effects should be considered when analyzing the magneto-optical response: (i) the contrast between the character confinement in the valence band induced by the strain field modulation along the stack and (ii) the elongation of the confinement sites that reduces the cylindrical symmetry of both QDs and QRs. We shall discuss the latter first.

To analyze the effects of increasing eccentricity in the electronic structure we must consider a model that includes the symmetry breakdown and magnetic field within the same framework. The in-plane potential profile used for both the QD and QR shape simulations is given by [23]

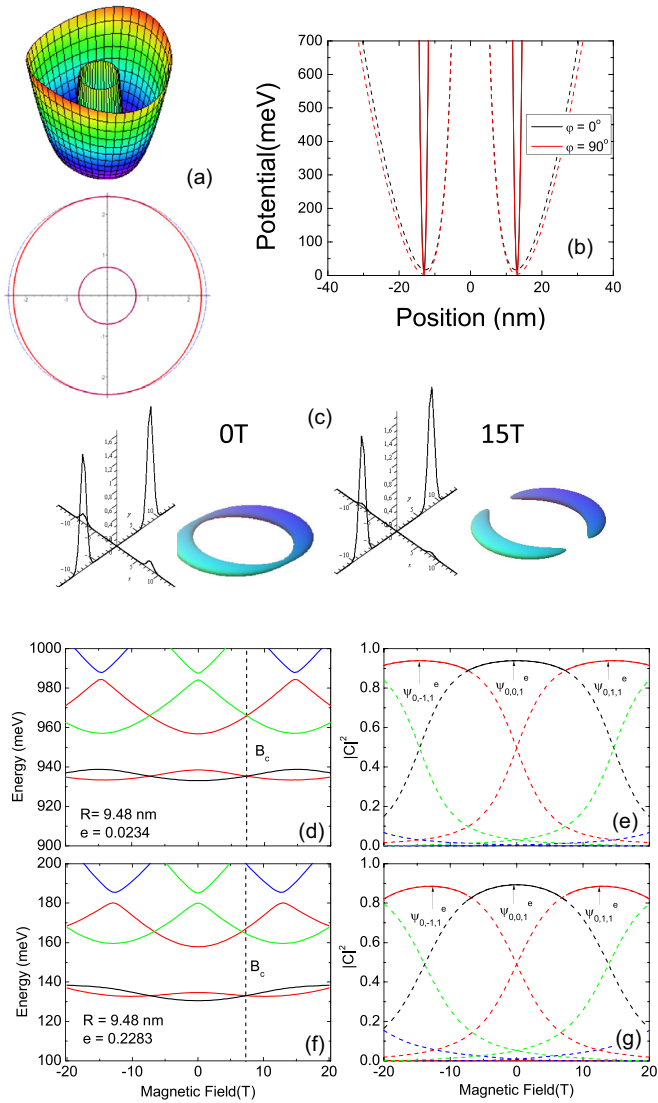$$V(r,\theta) = \frac{a_1}{r^2} + a_2 r^2 - 2\sqrt{a_1 a_2} + \delta r^2 \cos^2(\theta), \qquad (1)$$

FIG. 4. (Color online) (a) 3D lateral profile used to simulate the ring-shape confinement with the corresponding horizontal cross section in the lower panel: the solid curve represents the ring with eccentricity $e \neq 0$ and the dashed curve for $e = 0$. (b) Lateral QR profile for the two widths characterized in the simulations for two values of the angle θ. (c) The conduction band in-plane wave function of the ground state, $|\Phi^\delta(r,\theta,0)|^2$, and the corresponding electronic orbital, $|\Phi^\delta(r,\theta,z)|^2 = $ const, for two values of the magnetic field within an eccentric ring confinement, where the predominant character is $\psi_{0,0,0}^{(e)}$ at $B = 0$, and $\psi_{0,1,1}^{(e)}$ at $B = 15$ T. (d) Energy levels of an eccentric ring with $e = 0.0234$ in a magnetic field and (e) the corresponding wave-vector coefficients of the ground state. (f) Energy levels of an eccentric ring with $e = 0.2283$ in a magnetic field and (g) the corresponding wave-vector coefficients of the ground state.

as illustrated in Fig. 4(a). The parameters a_1 and a_2 are used to define the effective radius and width of the lateral confinement [23]. The corresponding material parameters of the ternary alloy, $In_xGa_{1-x}As$, were obtained by linear interpolation of the GaAs and the InAs values reported in Ref. [26] as $\gamma(x) = \gamma(GaAs) + x[\gamma(InAs) - \gamma(GaAs)]$. For the QD simulation, we set $a_1 = 0$ and $a_2 = 181.8$, while the QR was simulated with $a_1 = 147.5$ and $a_2 = 181.8$. The eccentricity

of the lateral confinement is given by $e = \sqrt{1 - a_2/(a_2 + \delta)}$ and the simulations will cover the limits of a broad and a narrow QR, as displayed in Fig. 4(b). The QR radius can be calculated as $R = (a_1/a_2)^{1/4}$ and the vertical confinement has been modeled by a rigid wall model. The solution for the 3D Schrödinger equation, $\Phi^\delta(r,\theta,z)$, corresponding to the potential profile in Eq. (1) can be expanded on the basis set, $\psi_{n,m,l}^{(e/h)}(r,\theta,z)$, of wave functions for $\delta = 0$, as described in Ref. [23],

$$\psi_{n,m,l}^{(e/h)}(r,\theta,z) = \phi_{n,m}^{(e/h)}(r,\theta)\chi_l^{(e/h)}(z)u_{e/h}, \qquad (2)$$

where $u_{e/h} = |j,m_j\rangle$ are the basis functions at the zone center in the Kane model: $|1/2,\pm1/2\rangle$, $|3/2,\pm3/2\rangle$, and $|3/2,\pm1/2\rangle$ for the electron, heavy-hole, and light-hole states, respectively. The planar wave function has the form

$$\phi_{n,m}^{(e/h)} = \frac{1}{\lambda_{(e/h)}} \left(\frac{\Gamma[n + M_{(e/h)} + 1]}{2^{M_{(e/h)}+1}n!(\Gamma[M_{(e/h)} + 1])^2\pi} \right)^{1/2}$$

$$\times \left(\frac{r}{\lambda_{(e/h)}} \right)^{M_{(e/h)}} e^{-im\theta} e^{-1/4(r/\lambda_{(e/h)})^2}$$

$$\times {}_1F_1\left(-n, M_{(e/h)} + 1, \frac{1}{2}(r/\lambda_{(e/h)})^2 \right), \qquad (3)$$

where ${}_1F_1$ is the hypergeometric function, $n = 0,1,2\ldots$, $m = 0,\pm1,\pm2,\ldots$, and the rigid wall function is

$$\chi_l^{(e/h)}(z) = \sqrt{\frac{2}{L}} \sin\left(\frac{l\pi z}{L} + \frac{l\pi}{2} \right), \qquad (4)$$

with $l = 1,2\ldots$. The corresponding eigenenergies are

$$E_{n,m,l}^{(e/h)} = \left(n + \frac{1}{2} + \frac{M_{(e/h)}}{2} \right) \hbar w_{(e/h)} - \frac{m}{2}\hbar w_{c(e/h)}$$

$$- \frac{\mu_{(e/h)}}{4} w_{0(e/h)}{}^2 r_0{}^2 + \left(\frac{l^2\pi^2\hbar^2}{2\mu_{(e/h)}L^2} \right), \qquad (5)$$

with $M_{(e/h)} = \sqrt{m^2 + \frac{2a_1\mu_{(e/h)}}{\hbar^2}}$, $\omega_{c(e/h)} = eB/\mu_{(e/h)}$, $\omega_{0(e/h)} = \sqrt{8a_2/\mu_{(e/h)}}$, $\omega_{(e/h)} = \sqrt{\omega_{c(e/h)}^2 + \omega_{0(e/h)}^2}$, $\lambda_{(e/h)} = \sqrt{\frac{\hbar}{\mu_{(e/h)}\omega_{(e/h)}}}$, and $\mu_{(e/h)}$ standing for electron and hole effective masses.

The results for the expansion on the basis $\Phi^\delta(r,\theta,z) = \sum_{n,m,l} C_{n,m,l}\psi_{n,m,l}^{HH}(r,\theta,z)$ are displayed in Fig. 4(c) for an eccentric confinement and two values of magnetic field. The broken rotational symmetry affects the wave function that shows a clear elongation as the eccentricity increases. The corresponding energy levels and ground state weight coefficients $C_{n,m,l}$ for the two profiles described in Fig. 4(b) are plotted in Figs. 4(d) and 4(e), and 4(f) and 4(g), respectively.

Note, in Figs. 4(d) and 4(f), the oscillations of the ground state energy as the magnetic flux increases. As expected, at certain critical fields B_c, where $\sqrt{\hbar/eB_c} = R$, the ground state changes character transiting through branches of increasing values of the angular momentum m. Yet, m is no longer a good quantum number for an eccentric confinement due to the coupling of unperturbed levels that follow the selection rules, $\Delta m = \pm2$. The actual character of the ground state, determined by the weight coefficients of the linear expansion for $e \neq 0$ is shown in Figs. 4(e) and 4(g). For increased eccentricity, as compared to Figs. 4 (d) and 4(f), the ground
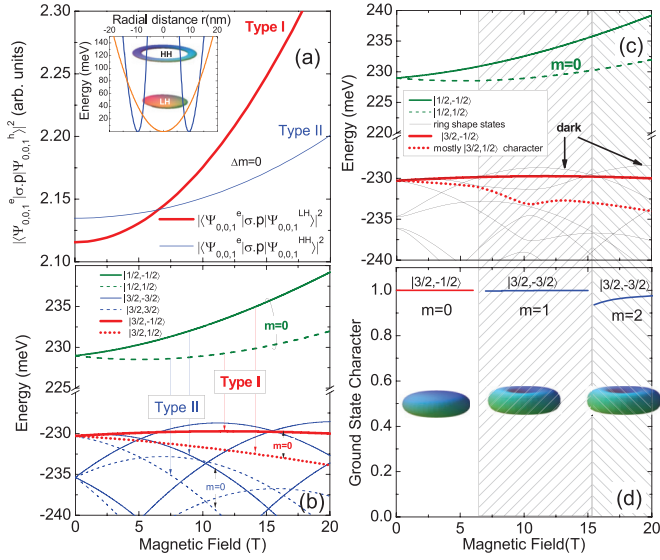
FIG. 5. (Color online) (a) The optical transition matrix elements involving the $m = 0$ HH and LH states of a QD with $R = 9.48$ nm and 6 nm height as a function of the magnetic field in the parabolic band approximation. The lateral QD profiles for the HH and LH subbands with a HH in the outer rim and a LH confined inside are shown in the inset. (b) The corresponding upper valence band and lower conduction band states (measured from above the energy gap) in a QD with HH in the outer rim and the electrons and LH confined inside as a function of the magnetic field in the parabolic band approximation. (c) The corresponding energy levels of a similar QD now with $e = 0.104$ calculated within the 4×4 Luttinger model [23].

state energy oscillation decreases while the angular momentum character remains oscillatory with the state hybridization increasing due to stronger interlevel coupling. However, even for highly eccentric confinements, the magnetic field cannot induce a sudden change in the state character at a certain

critical field that would lead to sharp differences in both the energy shift and the oscillator strength. Therefore, eccentricity effects alone cannot account for the peculiar optical response of the QD emission under magnetic field, as observed in the experimental measurements.

This peculiarity can only be expected when analyzing the differences between the HH and LH confinement potential profiles and the tuning of the ground state character of the valence band with the magnetic field. As simulated from the strain profile, the valence band has a type-I character for the LH and type-II character for the HH, due to the strain field modulation, as shown in Fig. 1(c). The details of the transformation on valence band due to the combination of strain profiles, spatial and magnetic confinements, as well as interdot coupling are given in a number of reported studies [27–29]. The magnetic tuning of the valence band character (HH or LH) in QDs has already been reported experimentally and confirmed theoretically [30,31]. The physical explanation for the origin of the type-I to type-II transition with magnetic field in the valence band of III-V QDs was given in Ref. [27]. The in-plane potential profile used to theoretically simulate the effect displayed in Fig. 1(c) is shown in Fig. 5(a).

Before detailing aspects of the peculiar valence band electronic structure, it is crucial to discuss the relative probability for an electron-hole pair recombination involving either a heavy-hole state confined nearby the outer rim of the QD or a light-hole state in the internal part of the ring. The optical oscillator strength for the electron-hole pair recombination from the conduction band ground state with $\delta = 0$ and $l = 1$ is proportional to

$$\left| \langle \psi^e_{n,m,1} | \hat{\sigma}^{\pm} \hat{p} | \psi^h_{n,m,1} \rangle \right|^2 = \left| \langle \phi^e_{n,m} | \phi^h_{n,m} \rangle \right|^2 |\langle u_e | \hat{\sigma}^{\pm} \hat{p} | u_h \rangle|^2, \quad (6)$$

where $\hat{\sigma}^{\pm} = 1/\sqrt{2}(\hat{x} \pm i\hat{y})$ is the light polarization and the overlap integral can be calculated as

$$\langle \phi^e_{n,m} | \phi^h_{n,m} \rangle = 2\pi \left(\frac{\Gamma[n + M_{(e)} + 1]}{2^{M_{(e)}+1} n! \Gamma[M_{(e)} + 1]^2 \pi} \right)^{1/2} \frac{\lambda^{M_{(e)}+1}_{(h)}}{\lambda^{M_{(e)}+1}_{(e)}} \left(\frac{\Gamma[n + M_{(h)} + 1]}{2^{M_{(h)}+1} n! \Gamma[M_{(h)} + 1]^2 \pi} \right)^{1/2} \int_0^\infty e^{-(r'^2/4)[(\lambda^2_{(h)}/\lambda^2_{(e)})+1]}$$

$$\times r'^{(M_{(h)}+M_{(e)}+1)} {}_1F_1 \left(-n, M_{(e)} + 1, \frac{1}{2} \left(r' \frac{\lambda_{(h)}}{\lambda_{(e)}} \right)^2 \right) {}_1F_1 \left(-n, M_{(h)} + 1, \frac{1}{2} r'^2 \right) dr'. \quad (7)$$

The numerical integration along the radial coordinate in Eq. (7) was taken up to 30–40 nm (according to the electronic state) attaining a good convergence. By taking into account that $|\langle u_e | \hat{\sigma}^{\pm} \hat{p} | u_{LH} \rangle|^2 = 1/3 |\langle u_e | \hat{\sigma}^{\pm} \hat{p} | u_{LH} \rangle|^2$, the matrix elements $|\langle \psi^e_{0,0,1} | \hat{\sigma}^{\pm} \hat{p} | \psi^h_{0,0,1} \rangle|^2$ were calculated for the spatial potential profiles with $e = 0$ and no valence band mixing as displayed in Fig. 5(a). In these configurations, a crossing between e-HH and e-LH transition intensity would be expected at intermediary field $B \simeq 6$ T. Yet, the type-II e-HH optically allowed transition (from the $m = 0$ conduction band ground state to the $m = 0$ valence band levels) is not energetically favorable as depicted in Fig. 5(b). Thus, the main transition observed in the QD photoluminescence should be type I since the energetically favorable states for type-II recombination

correspond to $m = 1$ and $m = 2$ valence band states, forbidden for transitions from the $m = 0$ electron ground state. In the case of a type-I to type-II optical transition induced by magnetic field, it would also be expected to detect a shift in the energy position of the emission energy of the value of $g^* \mu_B B$ (with g^* the electron effective Landé factor) due to the sudden change from LH to HH selection rules as the field increases. This is not, however, observed in Fig. 3(c), where only a kink of the diamagnetic shift of the QD emission is perceptible.

The character change between hole states, apparent energetically in the valence band ground state of the QD, is again illustrated in Fig. 5(c), where we tested the result beyond the parabolic band approximation within a Luttinger model

as described in Ref. [23] to assess the relative effect of the proximity of both valence subbands and the potential selection rule relaxation due to level mixing. A small eccentricity, $e = 0.104$, has also been added within the range used for the QR calculations. Despite the appearance of some anticrossings, there are no important contrasts between Figs. 5(b) and 5(c). The reduced overlap of the HH and LH wave functions, displayed in Fig. 5(d) weaken the intersubband mixing. The character coefficients of the main basis components of the valence band ground state are also shown in Fig. 5(d) where it is proven that, beyond 6 T, dark excitons are formed and this has an impact on the optical transition rates as discussed in Ref. [13]. To complement this characterization, the wave function of the valence band ground state has been drawn for magnetic fields: 5, 10, and 20 T.

The variations of the PL intensity with the magnetic field in Fig. 3(f) can be ascribed to the energy crossing around 6 T, where the character changes between LH and HH and, given the angular momentum modulation of the HH ground state, a bright-to-dark transition takes place according to the valence band occupancy [13]. It can also be noted that the strength of this effect is undoubtedly stronger for one of the spins. The effect of the bright-to-dark crossing contributes to a decrease of the photoluminescence after 6 T where the LH and HH levels cross.

V. CONCLUSIONS

In summary, we have investigated hybrid structures where InGaAs/GaAs QRs are grown over a vertical superlattice of laterally aligned InGaAs/GaAs QDs. Rather different oscillations of PL intensity of circular polarized emissions were detected in the spectral range of the QD radiation for increasing magnetic field. These oscillations are observed together with PL oscillations related to the AB interferences in the range of QR emissions. Such a behavior of the magneto-PL is interpreted in terms of joint effects associated to strain, spatial, and magnetic field confinement on the valence band forming the magnetoexciton ground state of the hybrid structure. Two possible effects that could lead to different field dependence were studied: eccentricity of the confinement and strain induced different profiles for HH and LH carriers. We demonstrated that the spin-dependent modulation of the intensity of the QD emission is weighted by the bright-to-dark crossing when the character of the valence band ground state evolves from type-I LH to a type-II HH. We hope these findings may be further explored in many different samples.

[1] V. P. Kunets, M. R. S. Dias, T. Rembert, M. E. Ware, Y. I. Mazur, V. Lopez-Richard, H. A. Mantooth, G. E. Marques, and G. J. Salamo, J. Appl. Phys. **113**, 183709 (2013).

[2] Y. I. Mazur, V. G. Dorogan, J. E. Marega, G. G. Tarasov, D. F. Cesar, V. Lopez-Richard, G. E. Marques, and G. J. Salamo, Appl. Phys. Lett. **94**, 123112 (2009).

[3] D. F. Cesar, M. D. Teodoro, V. Lopez-Richard, G. E. Marques, E. Marega, Jr., V. G. Dorogan, Y. I. Mazur, and G. J. Salamo, Phys. Rev. B **83**, 195307 (2011).

[4] Z. M. Wang, K. Holmes, Y. I. Mazur, and G. J. Salamo, Appl. Phys. Lett. **84**, 1931 (2004).

[5] H. Wen, Z. M. Wang, and G. J. Salamo, Appl. Phys. Lett. **84**, 1756 (2004).

[6] J. L. Baker, A. Widmer-Cooper, M. F. Toney, P. Geissler, and A. P. Alivisatos, Nano Lett. **10**, 195 (2010).

[7] Y. Chang, S. Jian, and J. Juang, Nanoscale Res. Lett. **5**, 1456 (2010).

[8] Z. Fan, H. Razavi, J.-W. Do, A. Moriwaki, O. Ergen, Y.-L. Chueh, P. W. Leu, J. C. Ho, T. Takahashi, L. A. Reichertz, S. Neale *et al.*, Nat. Mater. **8**, 648 (2009).

[9] Y. I. Mazur, V. G. Dorogan, E. Marega, Jr., P. M. Lytvyn, Z. Y. Zhuchenko, G. G. Tarasov, and G. J. Salamo, New J. Phys. **11**, 043022 (2009).

[10] J. Wu, Z. M. Wang, K. Holmes, E. Marega, Jr., Z. Zhou, H. Li, Y. I. Mazur, and G. J. Salamo, Appl. Phys. Lett. **100**, 203117 (2012).

[11] J. Wu, Z. M. Wang, K. Holmes, E. Marega, Jr., Y. I. Mazur, and G. J. Salamo, J. Nanopart. Res. **14**, 919 (2012).

[12] N. A. J. M. Kleemans, I. Bominaar-Silkens, V. M. Fomin, V. N. Gladilin, D. Granados, A. Taboada, J. M. Garcia, P. Offermans, U. Zeitler, P. M. Christianen *et al.*, Phys. Rev. Lett. **99**, 146808 (2007).

[13] A. O. Govorov, S. E. Ulloa, K. Karrai, and R. J. Warburton, Phys. Rev. B **66**, 081309 (2002).

[14] A. V. Chaplik, Pis'ma Zh. Eksp. Teor. Fiz. **62**, 885 (1995) [JETP Lett. **62**, 900 (1995)].

[15] R. A. Römer and M. E. Raikh, Phys. Rev. B **62**, 7045 (2000).

[16] M. D. Teodoro, V. L. Campo, Jr., V. Lopez-Richard, E. Marega, Jr., G. E. Marques, Y. Galvão Gobato, F. Iikawa, M. J. S. P. Brasil, Z. AbuWaar, V. G. Dorogan *et al.*, Phys. Rev. Lett. **104**, 086401 (2010).

[17] C. González-Santander, F. Domínguez-Adame, and R. A. Römer, Phys. Rev. B **84**, 235103 (2011).

[18] I. R. Sellers, V. R. Whiteside, I. L. Kuskovsky, A. O. Govorov, and B. D. McCombe, Phys. Rev. Lett. **100**, 136405 (2008).

[19] T. Benabbas, Y. Androussi, and A. Lefebvre, J. Appl. Phys. **86**, 1945 (1999).

[20] J. Stangl, V. Holy, and G. Bauer, Rev. Mod. Phys. **76**, 725 (2004).

[21] Calvin Yi-Ping Chao and S. L. Chuang, Phys. Rev. B **46**, 4110 (1992).

[22] Z. M. Wang, Y. I. Mazur, S. Seydmohamadi, G. J. Salamo, and H. Kissel, Appl. Phys. Lett. **87**, 213105 (2005).

[23] M. D. Teodoro, A. Malachias, V. Lopes-Oliveira, D. F. Cesar, V. Lopez-Richard, G. E. Marques, E. Marega, Jr., M. Benamara, Y. I. Mazur, and G. J. Salamo, J. Appl. Phys. **112**, 014319 (2012).

[24] Y. I. Mazur, V. G. Dorogan, M. E. Ware, E. Marega, Jr., P. M. Lytvyn, Z. Y. Zhuchenko, G. G. Tarasov, and G. J. Salamo, J. Appl. Phys. **112**, 084314 (2012).

[25] D. Haft, C. Schulhauser, A. O. Govorov, R. J. Warburton, K. Karrai, J. M. Garcia, W. Schoenfeld, and P. M. Petroff, Physica E **13**, 165 (2002).

[26] I. Vurgaftman, J. R. Meyer, and L. R. Ram-Mohan, J. Appl. Phys. **89**, 5815 (2001).

[27] M. Tadic', F. M. Peeters, and K. L. Janssens, Phys. Rev. B **65**, 165333 (2002).

[28] K. L. Janssens, B. Partoens, and F. M. Peeters, Phys. Rev. B **67**, 235325 (2003).

[29] L. Villegas-Lelovsky, M. D. Teodoro, V. Lopez-Richard, C. Calseverino, A. Malachias, E. Marega, Jr., B. L. Liang, Y. I. Mazur, G. E. Marques, C. Trallero-Giner *et al.*, Nanoscale Res. Lett. **6**, 56 (2010).

[30] E. Margapoti, F. M. Alves, S. Mahapatra, T. Schmidt, V. Lopez-Richard, C. Destefani, E. Menendez-Proupin, F. Qu, C. Bougerol, K. Brunner *et al.*, Phys. Rev. B **82**, 205318 (2010).

[31] E. Margapoti, F. M. Alves, S. Mahapatra, T. Schmidt, V. Lopez-Richard, C. Destefani, E. Menendez-Proupin, F. Qu, C. Bougerol, K. Brunner *et al.*, New J. Phys. **14**, 043038 (2012).